

1 **PV power modelling using solar radiation from ground-based**
2 **measurements and CAMS: Assessing the diffuse component related**
3 **uncertainties leveraging the Global Solar Energy Estimator (GSEE)**

4 Nikolaos Papadimitriou^{1,2}, Ilias Fountoulakis², Antonis Gkikas², Kyriakoula
5 Papachristopoulou³, Andreas Kazantzidis¹, Stelios Kazadzis³, Stefan Pfenninger⁴, John
6 Kapsomenakis², Kostas Eleftheratos^{5,6}, Athanassios A. Argiriou¹, Lionel Doppler⁷, and
7 Christos S. Zerefos^{2,6,8,9}

8 ¹Department of Physics, University of Patras, 26500 Patras, Greece

9 ²Research Centre for Atmospheric Physics and Climatology, Academy of Athens, 11521 Athens,
10 Greece

11 ³Physikalisch-Meteorologisches Observatorium Davos, World Radiation Center (PMOD/WRC), 7260
12 Davos, Switzerland

13 ⁴Faculty of Technology, Policy, and Management (TPM), Delft University of Technology, 2628 BX
14 Delft, the Netherlands

15 ⁵Department of Geology and Geoenvironment, National and Kapodistrian University of Athens,
16 15784 Athens, Greece

17 ⁶Biomedical Research Foundation, Academy of Athens, 11527 Athens, Greece

18 ⁷Deutscher Wetterdienst, Meteorologisches Observatorium Lindenberg – Richard Assman
19 Observatorium (DWD, MOL-RAO), 15848 Lindenberg (Tauche), Germany

20 ⁸Navarino Environmental Observatory (N.E.O.), 24001 Messinia, Greece

21 ⁹Mariolopoulos-Kanaginis Foundation for the Environmental Sciences, 10675 Athens, Greece

22 Corresponding author: Nikolaos Papadimitriou (npapadimitriou@academyofathens.gr, Vasilissis
23 Sofias 79, 11521 Athens, Greece)

24 **Abstract**

25 Accurate PV power production modelling requires precise knowledge of the distribution of solar
26 irradiance among its direct and diffuse components. Since this information is rarely available, this

27 requirement can be addressed through the use of diffuse fraction models. In this study, we try to
28 quantify the errors in PV modelling when measurements of the diffuse solar irradiance are not
29 available. For this purpose, we use total and diffuse solar irradiance data obtained from ground-
30 based measurements of BSRN to simulate the PV electric output using GSEE. We have chosen five
31 sites in Europe and North Africa, with different prevailing conditions, where BSRN measurements are
32 available. GSEE incorporates an implementation of the [Boland-Ridley-Lauret \(BRL\)](#) diffuse fraction
33 model, along with a Climate Data Interface that enables simulations across different time scales.
34 We evaluate the capability of BRL in providing accurate estimations of the diffuse fraction under
35 diverse atmospheric conditions, with particular attention on the presence of clouds and aerosols
36 and assess the extent to which its associated errors propagate to energy production modelling.
37 Furthermore, we compare GSEE outputs when using CAMS radiation time-series as input instead of
38 ground-based measurements, to quantify the impact of the CAMS radiation product uncertainties in
39 PV modelling.

40 **Keywords**

41 Solar energy modelling; CAMS radiation; PV power modelling; aerosol; dust; solar radiation

42 **1. Introduction**

43 Decarbonizing the power sector in a sustainable manner is pivotal in the effort to mitigate climate
44 change (Edenhofer et al., 2011; Owusu & Asumadu-Sarkodie, 2016; IPCC, 2023) and the large-scale
45 deployment of Solar Energy offers significant prospects toward this objective (Kakran et al., 2024).
46 The available solar energy is a variable source, fluctuating across different timescales with a unique
47 solar-resource profile over individual locations (McMahan et al., 2013). Therefore, accurate solar
48 energy forecasting and resource assessment is crucial for minimizing the risk in selecting project
49 location, designing the appropriate solar-energy conversion technology, and integrating new sources
50 of solar based power generation into the electricity grid (Stoffel, 2013), while short-term, intra-hour
51 forecasts are critical for power plant operations, grid-balancing, real-time unit dispatching,
52 automatic generation control, and trading (Pedro et al., 2017).

53 ~~For practical reasons, it is critical to extend Extending solar irradiance forecasting to encompass~~
54 ~~methods linked to solar-based power generation derive~~ PV power forecasts ~~is essential in solar~~
55 ~~energy applications. PV power modelling~~ can be ~~derived achieved~~ through the following additional
56 steps to solar irradiance forecasting: (i) decomposing Global Horizontal Irradiance (GHI) into Diffuse

57 Horizontal Irradiance (DHI) and Direct Normal Irradiance (DNI)); (ii) calculating the plane-of-array
58 irradiance incident on the surface of PV planes, whether static or mounted on a solar tracking
59 system, and (iii) simulating the PV power production primarily based on the in-plane irradiance
60 (Blanc et al., 2017).

61 The scarcity of concurrent measurements of both solar irradiance components, coupled with the
62 complexity of their theoretical computation, has driven the development of numerous empirical
63 models for estimating the diffuse fraction (ratio of the diffuse-to-global solar radiation). A seminal
64 contribution in this area was made by Liu and Jordan (1960), who established a correlation between
65 the diffuse fraction and the clearness or cloudiness index (ratio of the global-to-extraterrestrial
66 radiation). These models predominantly rely on the clearness index as the principal predictor. They
67 are generally classified into single-predictor models and multi-predictor models, with the latter
68 incorporating additional astronomical variables for enhanced precision (Paulescu & Blaga, 2019).
69 Typically, these models are expressed as polynomial equations, ranging from the 1st to the 4th degree,
70 that link the diffuse fraction to the clearness index (Jacovides et al., 2006). $DF = f(\text{clearness index},$
71 ** params*) (Jacovides et al., 2006). Boland et al. (2001) proposed the use of a logistic function
72 instead of linear or simple nonlinear functions of the clearness index. Ridley et al. (2010) developed
73 a multiple-predictor logistic model, known as the Boland-Ridley-Lauret (BRL), which combines
74 simplicity and reliable performance across both the Northern and Southern Hemispheres. The BRL
75 model extends Boland's approach by adopting the hourly clearness index as the principal predictor
76 and introducing the following additional parameters: apparent solar time, daily clearness index, solar
77 altitude, and a measure of the persistence of global radiation level. In the implementation of the BRL
78 included in the GSEE, the users set as input only the hourly clearness. Moreover, this implementation
79 adopts the updated parameters proposed by Lauret et al. (2013), which derived using data from nine
80 worldwide locations covering a variety of climates and environments across Europe, Africa, Australia
81 and Asia. While the existing models consider all-sky conditions, in solar energy modelling it is critical
82 to focus on cloud-free skies, where energy production is maximized. Under such conditions,
83 aerosols become the primary parameter influencing the distribution of solar irradiance among its
84 components. (e.g., Blaga et al., 2024). Specifically, the BRL model accounts for aerosols indirectly
85 through the clearness index, which is indicative of the overall atmospheric attenuation of solar
86 radiation.

87 ~~Regions~~In regions dominated by abundant sunshine, such as the Mediterranean and Middle East,
88 which are favorable for solar based power generation, the attenuation of solar irradiance is strongly
89 influenced by aerosols, and particularly desert dust aerosols. Several studies highlighted the impact
90 of desert dust aerosol in the downwelling solar irradiance and the energy production in these regions
91 (Fountoulakis et al., 2021; Papachristopoulou et al., 2022);Kosmopoulos et al., 2018; Kouklaki et
92 al., 2023. The significance of considering the effect of aerosols in short-term solar irradiance
93 forecasting and nowcasting is emphasized by Kazantzidis et al. (2017),Raptis et al. (2023) and
94 Papachristopoulou et al. (2024).

95 The Global Solar Energy Estimator (GSEE; Pfenninger & Staffell, 2016) is a widely used open access
96 model for simulating PV power output, designed for rapid calculations and ease of use~~;~~.It comes
97 with an implementation of the BRL diffuse fraction model (Ridley et al., 2010; Lauret et al., 2013).

98 While PV power modelling is essential for linking solar resources to energy production, the existing
99 literature does not adequately address its reliability under diverse atmospheric conditions. To the
100 best of our knowledge, the existing literature does not include studies that explicitly address the
101 uncertainties in PV energy production modeling associated with the partitioning of solar radiation
102 into its direct and diffuse components at the model input. In this study, we supply GSEE with input
103 data from ground-based measurements as well as from the Copernicus Atmospheric Monitoring
104 Service (CAMS), aiming to investigate differences in PV power output simulations, which arise from
105 providing only GHI as input radiation data. At the outset, we focus on evaluating the reliability of BRL
106 under diverse atmospheric conditions, with particular attention to the dependence of its accuracy
107 on the presence of clouds and aerosols. To further explore this, we conduct a sensitivity analysis
108 using radiative transfer model (RTM) simulations under cloud-free skies. Following these analyses,
109 we assess the extent to which the associated uncertainties in the estimation of the diffuse fraction
110 spread to the power generation over hourly intervals. This step involves simulating PV plants with
111 varying configurations.

112 GSEE is also effective for analyzing trends and variability in solar based power generation through its
113 climate interface submodule (e.g., Hou et al., 2021~~;~~),where the BRL model is integrated within the
114 internal processing chain The accuracy of the climate interface in estimating the total daily PV power
115 output is also evaluated in this study.

116

117 **2. Data and Methodology**

118 2.1 Global Solar Energy Estimator (GSEE)

119 The modelling of the PV power output is conducted using the version 0.3.1 of GSEE (Pfenninger &
120 Staffell, 2016). The model features functions for simulating a complete PV system, incorporating
121 characteristics and specifications such as location, installed capacity, technology, tracking (fixed, 1-
122 axis, 2-axis), tilt angle, and orientation.

123 The user provides as input time-series data of solar radiation, and optionally, ambient air
124 temperature and surface albedo. Specifically, the model requires GHI and, when available, the
125 Diffuse Fraction. If the diffuse component is not provided, the provided implementation of the BRL
126 diffuse fraction model (Ridley et al., 2010; Lauret et al., 2013) is employed to estimate it, relying only
127 on time-series of the hourly clearness index and the geographical coordinates. While in the single-
128 site application of the GSEE model with hourly time resolution the user has the option to adjust the
129 input and select alternative diffuse fraction models implemented by external libraries, e.g., pvlib
130 (Anderson et al., 2013), the climate data interface automatically invokes the BRL model as part of the
131 internal processing workflow. GSEE utilizes the provided information for the distribution of the
132 irradiance components and applies trigonometric calculations to determine the total solar
133 irradiance incident on the panel's inclined plane. More precisely, for the plane-of -array irradiance
134 calculation a GSEE includes the submodule "trigon" (transposition model), which is based on
135 trigonometric formulations, that account of the surface albedo, thereby including the ground-
136 reflected component of solar radiation. However, the transposition model is integrated within the
137 GSEE internal algorithms, so it cannot be modified by the user.

138 After solar irradiance the most significant parameter regarding energy production is air temperature
139 (e.g., Dubey et al., 2013). If temperature is not provided by the user, the model assumes a default
140 value of 20 °C. In this study, temperature was used as input only in the simulations with BSRN data,
141 as it is provided alongside actinometric radiation measurements. A surface albedo value of 0.3
142 considered by default from the model, introduces some uncertainty in our simulations, which
143 however is estimated to be small. Under cloudless conditions, a 10% difference in surface albedo
144 changes the GHI by ~1% for SZA < 75°. Differences are larger under cloudy conditions (~ 10%
145 difference in GHI for a 10% difference in surface albedo). Nevertheless, surface albedo at the
146 selected sites is generally low and relatively invariant throughout the year (even at the most northern

147 site of Lindenberg there is only a limited number of days with increased surface albedo due to snow
148 cover).

149 The available options for the panel type are crystalline silicon (c-Si) and Cadmium Telluride (CdTe),
150 where the power output is modeled based on the relative PV performance model described by Huld
151 et al. (2010). For fixed panels, a built-in latitude dependent function for the optimal tilt is also
152 included.

153 Moreover, GSEE includes a Climate Data Interface submodule that enables the processing of gridded
154 climate datasets, with varying temporal resolutions, ranging from hourly to annual. Within the
155 context of this submodule, the use of BRL serves as part of the resampling and upsampling
156 processes applied to input climate datasets with daily resolution. For processing data with lower-
157 than-daily resolutions, it incorporates the use of Probability Density Functions (PDFs), which
158 describe the probability with which a day with a certain amount of radiation occurs within a month
159 (Renewables Ninja, n.d.). This methodology accounts for the non-linear distribution of mean monthly
160 radiation across individual days, ensuring a more representative temporal disaggregation. The
161 processes applied to the mean daily irradiance are described in detail in Section 3.4.

162 For the purposes of this study, we simulated solar plants with capacity of 1 kWp, and for both
163 available technologies. The simulations with c-Si technology, considered as default by the model,
164 are presented ~~detailed~~ in detail the following sections. The results of the simulations with CdTe
165 technology are provided in the supplement, and are not thoroughly discussed, since they are very
166 similar to the results for the c-Si technology. Regarding the mounting approach, the solar plants were
167 either static and oriented to the south or equipped with a 2-axis solar tracking system. In the case of
168 fixed panels, we selected the optimal tilt angle relying on the latitude dependent built-in function.

169 The input parameters defining the characteristics of the simulated PV plants are summarized in Table
170 1.

171 **Table 1.** Input parameters defining the characteristics of the simulated PV plants

Capacity	Mounting Approach		Technology	
1 kWp	Fixed	2-axis tracking	c-Si	CdTe

	Orientation: south	Tilt Angle: $f(\text{latitude})$ built-in function for optimal tilt			
--	-----------------------	---	--	--	--

172

173 **2.2 Ground-based measurements**

174 We supplied GSEE with ground-based irradiance as well as ambient temperature measurements
 175 collected from five stations of the Baseline Surface Radiation Network (BSRN; Driemel et al., 2018).
 176 Moreover, information about aerosols was retrieved from co-located stations of the Aerosol Robotic
 177 Network (AERONET; Holben et al., 1998; Dubovik et al., 2000).

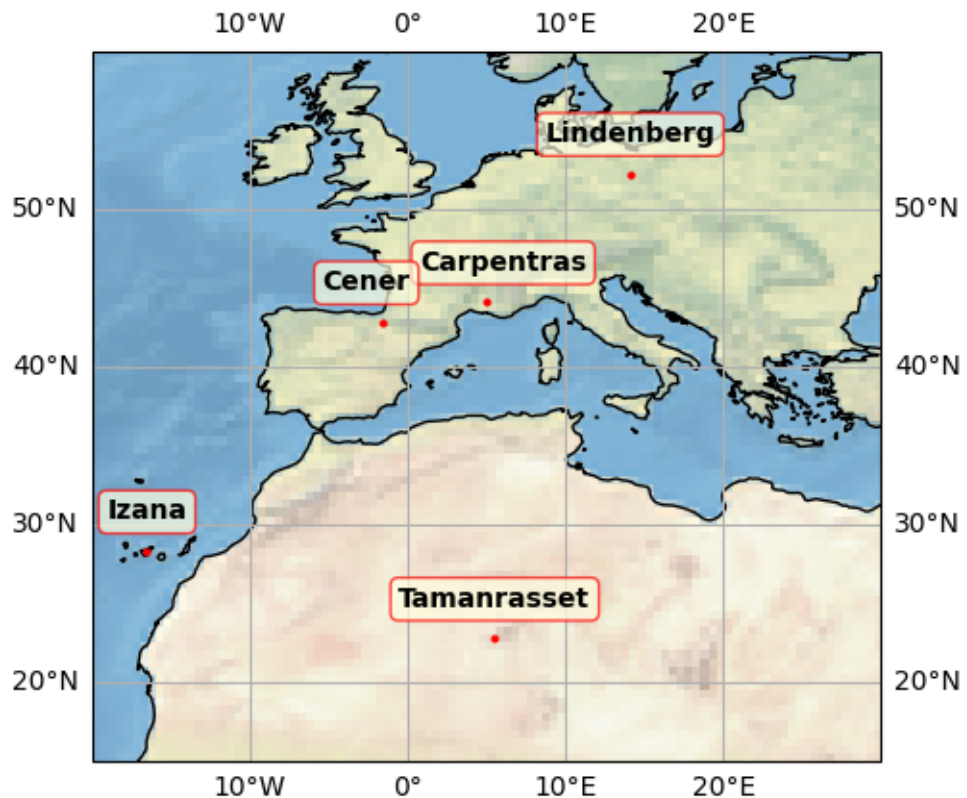
178 Information for the stations utilized for this study is summarized in Table 2, and their geographical
 179 location is depicted in Figure 1.

180

181 **Table 2.** Detailed information about the location of the ground-based stations used in this study.

STATION	Latitude [° N]	Longitude [° E]	Elevation [m]
Carpentras (CAR)	44.08	5.06	100
Cener (CNR)	42.82	-1.60	471
Izaña (IZA)	28.31	-16.50	2373
Lindenberg (LIN)	52.21	14.12	125
Tamanrasset (TAM)	22.79	5.53	1385

182



183

184 **Figure 1.** Locations of the BSRN and co-located AERONET stations that are used in the current
185 study

186

187 BSRN station-to-archive files were accessed and manipulated using the SolarData v1.1 R package
188 (Yang, 2019), and the BSRN-recommended quality check (QC) tests (Long & Dutton, 2010) applied
189 to the collected data. Some data gaps arose due to measurements removed during the QC
190 procedure. Although these data gaps are, in most cases, shorter than 2-3 hours, they may affect the
191 BRL performance throughout the corresponding days. Consequently, days affected by such data
192 gaps excluded from the analysis. We retrieved data for 2017, with 1-minute temporal resolution. We
193 used GHI, DHI, and Temperature as inputs to the GSEE model. Initially, the data were resampled to
194 hourly, and and mean hourly values of GHI and DHI are calculated. Then, the simulations were
195 conducted using either GHI and DHI, or only GHI along with the deployment of BRL. The input to BRL
196 consists of hourly clearness index, derived by dividing GHI measurements with the solar radiation

197 incident on a horizontal plane at the Top of the Atmosphere (TOA) above the examined location.
198 Subsequently, the 1-min timeseries resampled also to a daily resolution and transformed into three-
199 dimensional arrays, $GHI = f(\text{time}, \text{lat}, \text{lon})$, where the spatial dimensions of each dataset
200 corresponded to a unique point defined by the coordinates of the associated station. Simulations
201 with the daily time-resolved dataset were performed using the Climate Data Interface.

202 Measurements Representing cloudiness is a challenging task that requires several observations. For
203 this purpose, aiming to obtain an indicative measure of the intra-hour cloudiness conditions we
204 adopted the following formulation. Specifically, measurements of Direct Normal Irradiance (DNI)
205 were utilized to obtain information for cloudiness relying on the conditions stated by WMO (2021),
206 according to which sunshine duration is the total period where DNI exceeds 120 W/m^2 . Alternative
207 approaches such as the Cloud Modification Factor, require estimates of the clear sky irradiance,
208 which introduces additional uncertainty. For the purpose of this analysis, we introduced a solar
209 visibility (SV) parameter. Specifically, we assigned the value 0 when sun was obscured and the value
210 1 when visible. Aiming to describe the mean intra-hour cloudiness conditions, we considered the
211 sky as cloud-free, cloudy, and partly cloudy based on the mean SV for the entire corresponding hour
212 as follows:

$$213 \langle SV \rangle_{\text{hour}} : \begin{cases} 1 & \text{cloud-free} \\ \in (0,1) & \text{partly cloudy} \\ 0 & \text{cloudy} \end{cases}$$

214 For aerosol information, we accessed the AERONET Version 3 (V3) (Giles et al., 2019) and retrieved
215 level 2.0 data (from direct sun measurements) for Aerosol Optical Depth at 500nm (AOD_{500}), which
216 serves as a representative measure of the aerosol load; Ångström Exponent between 440 and 870
217 nm wavelengths ($AE_{440-870}$), where values near 0 correspond to coarse dust particles and values
218 around 2 to fine (e.g., smoke) particles (Dubovik et al., 2002); and Fine Mode Fraction at 500nm
219 (FMF_{500}) obtained from the Spectral Deconvolution Algorithm (SDA) retrievals, to distinguish aerosol
220 into fine and coarse mode. The data were resampled at hourly intervals and a mean hourly value
221 calculated. After, the hourly mean values divided into clusters regarding AOD based on AOD_{500} ,
222 reflecting different levels of aerosol load and allowing us to quantify their impact on solar energy
223 production. To investigate the impact related exclusively to aerosols, we included only hours with
224 cloud-free sky conditions. The clusters are defined in detail as follows:

225 • $AOD_{500} \leq 0.05$: Low aerosol load

226 • $0.05 < AOD_{500} \leq 0.15$: Moderate aerosol load
227 • $0.15 < AOD_{500} \leq 0.3$: High aerosol load
228 • $AOD_{500} > 0.3$: Very high aerosol load

229 To evaluate the performance of the Climate Interface over daily intervals, we defined the sunny
230 (cloudless) days using the condition: $\langle SV \rangle_{day} \geq 0.9$. Next, to characterize the average aerosol
231 conditions on sunny days, we applied the following classification:

232 • $\langle AOD_{500} \rangle_{day} \leq 0.05$: very-low aerosol
233 • $\langle AOD_{500} \rangle_{day} > 0.05$: aerosol-laden

234 Detailed comparisons of the energy production over hourly and daily integrals-e under the various
235 predefined sky conditions are provided in the supplement through evaluation metrics.

236 The selected locations have quite different atmospheric conditions regarding cloudiness and
237 aerosols. Additionally, they vary in altitude. A brief overview of the prevailing conditions derived from
238 the ground-based data is provided on the supplement. Regarding cloudiness, it is notable that in
239 Lindenberg the sky is generally overcast, whereas in southern locations sunshine dominates. In
240 terms of aerosols, very high aerosol loads occur more frequently in Tamanrasset. As for aerosol type,
241 there is considerable variation among the examined locations: Carpentras, Cener, and Lindenberg
242 are primarily influenced by fine mode aerosols, while Tamanrasset and Izaña are mostly affected by
243 coarse mode aerosols.

244 For investigating the impact of desert dust aerosol in solar based power generation, Tamanrasset
245 serves as a representative and exceptional case because it is in a region with important sources of
246 Saharan dust aerosols (Faid et al., 2012). Meanwhile, Izaña, located in subtropical North Atlantic, is
247 a high mountain station within the free troposphere, affected-my mineral dust when the Saharan Air
248 Layer top exceeds the station height, especially through August to October (Toledano et al., 2018;
249 Cuevas et al., 2018). Due to its high altitude, Izaña avoids contamination from local or regional
250 sources (Barreto et al. 2022). The Canary Islands, where Izaña is located, are influenced by extreme
251 dust events that cause a significant decrease in PV power generation (Canadillas-Ramallo et al.,
252 2021). In South Europe, which is also affected by the transport of Saharan dust across the
253 Mediterranean, aerosol types exhibit a mixture as a result of simultaneous local pollution and low
254 concentration of mineral dust (Logothetis et al., 2020).

255 [2.3 Copernicus Atmospheric Monitoring Service \(CAMS\)](#)

256 We retrieved data from the CAMS radiation service (Schroedter-Homscheidt et al., 2022; Qu et al.,
257 2017), from the solar radiation time-series product (CAMS, 2020). The CAMS solar radiation service
258 provides historical estimates for global solar radiation, along with its components, from 2004 to
259 present. These values are provided with a frequency as fine as 1-minute. In this study, we used the
260 hourly time-series of GHI and DHI for all-sky conditions, setting the input coordinates to match the
261 locations of the BSRN stations. [The solar radiation time-series product \(CAMS, 2020\) performs](#)
262 [interpolations integrated in its internal algorithm and provides time-series for the coordinates and](#)
263 [the altitude of a single-site location.](#) We compared the solar energy production derived from the use
264 of CAMS data with that derived from the use of ground-based measurements from BSRN.

265 [2.4 Radiative Transfer Model \(RTM\)](#)

266 We performed Radiative Transfer (RT) simulations aiming to further assess the uncertainties in
267 estimating the diffuse fraction arising from the effect of aerosols. The simulations were conducted
268 using libRadtran (Emde et al., 2016; Mayer & Kylling, 2005), a widely used software package, allowing
269 the computation of radiances, irradiances, and actinic fluxes. A sensitivity analysis was performed
270 by comparing the diffuse irradiance calculated from libRadtran with the estimations of BRL. This
271 analysis examines the dependence of the aerosol-related discrepancy as function of Solar Zenith
272 Angle (SZA) and latitude, considering the effect of parameters such as surface albedo and altitude.
273 To conduct aerosol parameterizations, we considered the default aerosol extinction profile (Shettle,
274 1989) and set asymmetry factor (gg) to 0.7, while varying the Single Scattering Albedo (SSA) and the
275 Ångström Exponent (AE), and defining AOD_{500} by adjusting the value of the parameter-b in
276 Ångström's law (Ångström, 1929) as follows:

$$277 \quad \tau_\lambda = b \cdot \lambda^{-a} \rightarrow AOD_{500} = b \cdot (0.5 \mu m)^{-AE}$$

278 The standard aerosol profiles (Anderson et al., 1986) were used for all sites. According to
279 Fountoulakis et al. (2022), using a more accurate vertical distribution of aerosols in the troposphere
280 would have a negligible effect in the GHI and DHI at the Earth's surface.

281 Table 3 illustrates the libRadtran settings used in this study.

282 **Table 3.** LibRadtran inputs

Parameter	Input
Atmospheric profile	Mid-latitude summer (April-September)/mid-latitude winter (October - March) (Anderson et al., 1986)
Extraterrestrial spectrum	(Kato et al. 1999)
<u>SZA</u> <u>Datetime</u>	with step 90° date and time input accompanied by project location coordinates
Altitude	0.1/2 km
Surface albedo	0.2 / 0.8
Number of streams	6
RT solver	sdisort (Buras et al., 2011)
AE	0 – 2 with step 1
SSA	0.7, 0.9, 1.0
gg	0.7
TOC (Total Ozone Column)	300 DU
<u>Integrated</u> Water <u>vapor</u> <u>Vapor</u>	15 mm

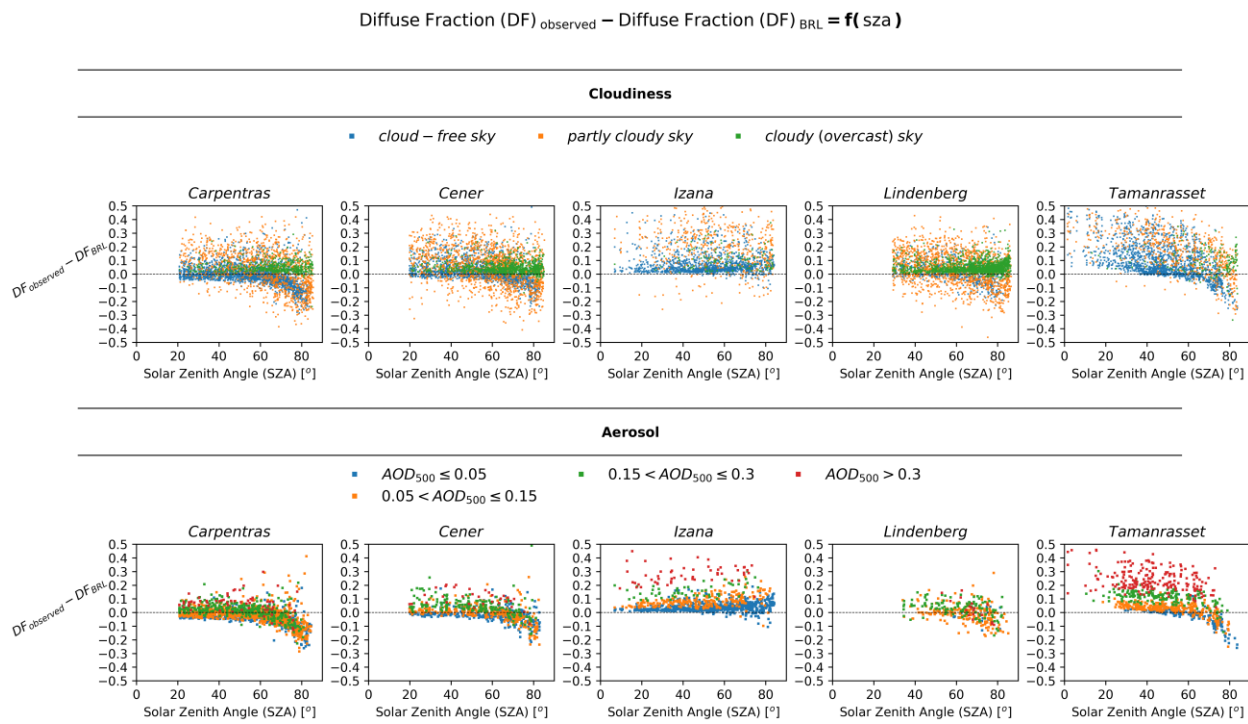
283

284 **3. Results**

285 3.1 Performance verification of the BRL diffuse fraction model

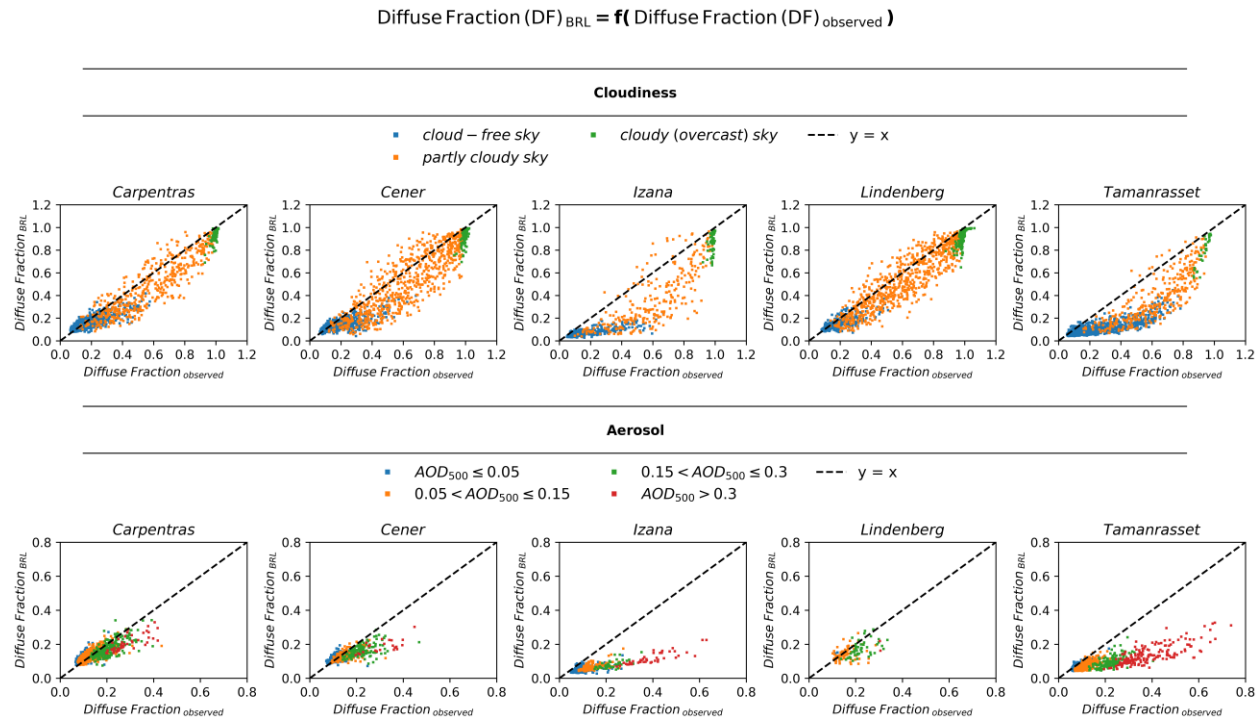
286 The performance of BRL was evaluated by comparing the actual diffuse fraction, obtained directly
 287 from resampled to hourly BSRN ground-based measurements, with that derived using BRL.
 288 ~~Initially~~As a first step, to isolate the influence of SZA from that associated with the atmospheric
 289 conditions, the difference in diffuse fraction (DF) between the observed and the one estimated using
 290 BRL as a function of SZA is presented in Figure 2. The atmospheric conditions are represented
 291 separately for both all-sky and cloud-free sky conditions and are grouped into clusters, as outlined
 292 in Section 2.2. The patterns reflecting the differences under the distinct sky conditions indicate an
 293 additional dependency on SZA, which becomes apparent approximately ~~beyond 60°~~at SZA between
 294 60° and 70°. In most cases, there is an almost constant displacement with respect to y=0 below 60°,

295 as well as a ~~negative trend~~ change in behavior when SZA exceeds this value. Izaña presents a special
 296 case, as the station is located at a very high altitude, ~~with adjacent clouds occasionally being~~
 297 ~~situated at a. At such high altitudes the contribution of the diffuse component to the total irradiance~~
 298 ~~is significantly smaller relative to~~ lower elevation than the station itself. As a result altitude sites,
 299 which seems to be captured more accurately by BRL at high SZAs. We must also note that (i) at Izaña,
 300 the actual diffuse irradiance ~~experiences~~ may experience an additional enhancement due to the
 301 contribution of ~~these~~ adjacent lower-lying clouds – an effect that is not accounted for in the diffuse
 302 fraction model, and (ii) during dust events the site is usually inside – and not under – the dust layer,
 303 which results in more complex interactions between dust and solar radiation relative to lower
 304 altitude sites. Defining an exact limit (for the lower altitude sites), where the behavior is changing, is
 305 challenging; therefore, 60° was selected for practical energy-related applications, focusing on
 306 periods with meaningful energy contribution, and is supported by the sensitivity analysis (Section
 307 3.2) under clear-sky conditions. Concerning the same grouped atmospheric conditions, Figure 3
 308 illustrates the comparison between the observed and the estimated diffuse fraction for $SZA \leq 60^\circ$.
 309 This approach allows us to examine BRL performance after eliminating the influence of SZA, thereby
 310 providing a more comprehensive view of its reliability.



311
 312 **Figure 2.** Difference between the ~~observed and the diffuse fraction~~ estimated by the ground-based
 313 measurements and by using the BRL diffuse fraction model as a function of SZA under diverse

314 atmospheric conditions: (top) classification with respect to cloudiness and (bottom) classification
315 with respect to aerosol optical depth



316

317 **Figure 3.** Comparison of the diffuse fraction estimated using BRL with the actual one calculated
318 directly from that estimated by the ground-based measurements under diverse atmospheric
319 conditions for SZA < 60°: (top) classification with respect to cloudiness and (bottom) classification
320 with respect to aerosol optical depth

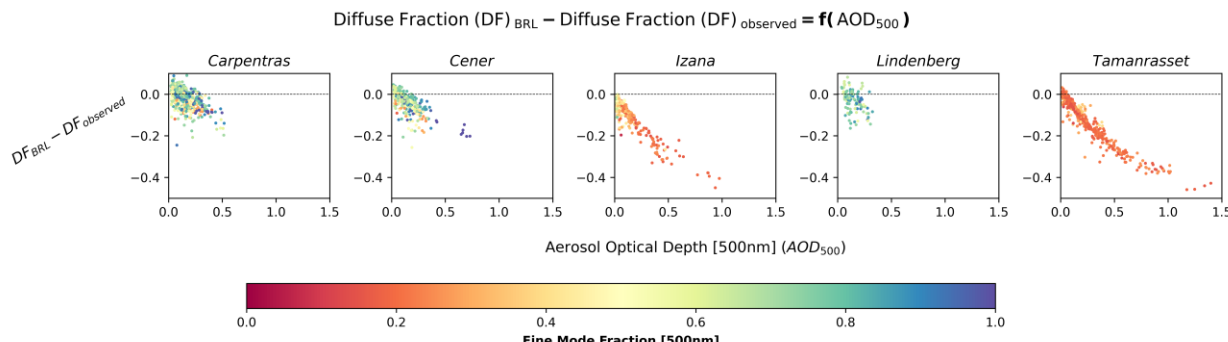
321

322 From Figure 3, a distinct dependency of BRL's reliability on the atmospheric conditions can be
323 observed. Under all-sky conditions, the presence of clouds has a notable impact on the
324 model's performance. Partly cloudy conditions result in greater dispersion of the values from
325 the identity line respectively, likely due to the complexity of such sky scenes. Under overcast
326 conditions, where the sky can be considered homogeneous and isotropic, the model performs
327 slightly better. However, the limitations of the DNI-based
328 classification methodology, related to the complexity of the cloud scenes, the spatiotemporal
329 variability during the hourly periods, and the 3D variability of cloud properties, would require
330 additional observational tools for a more detailed investigation. More specifically, the vast majority
331 of overcast cases where the BRL diffuse fraction is below 0.8 while the observed is close to 1

332 correspond to periods involving rapid transitions between partly cloudy and overcast skies, occurring
333 either during the hour itself or immediately before or after it. Furthermore, a limited number of cases
334 identified during intense dust events at Tamanrasset and Izana, where the reduction of DNI was so
335 pronounced that the applied DNI-based criterion classified these conditions as overcast. However,
336 these cases are not further investigated, as the energy production levels during such periods are very
337 low.

338 Under cloud-free skies, BRL tends to underestimate, and this bias becomes more pronounced as
339 aerosol load increases. Aiming to highlight this dependency, Figure 4 shows the difference between
340 the estimated and the observed diffuse fraction as function of AOD_{500} , emphasizing also the extent
341 to which it is related to the aerosol type by providing FMF_{500} . ~~A negative trend~~ A decrease for
342 increasing AOD_{500} is evident across all cases. In Tamanrasset and Izaña, associated with the
343 influence of Saharan dust, the coarse mode dominates, and a more distinct and well-defined curve
344 is depicted– compared to other sites.

345 It is important to clarify that for assessing the impact of aerosols we have assumed entirely cloud-
346 free conditions. However, the criterion applied based on DNI does not fully guarantee the absence of
347 small, scattered clouds within the sky dome. Such clouds could induce slight enhancements in DHI.
348 A more rigorous assessment of the impact associated exclusively with aerosols could be achieved
349 by integrating images from ground-based co-located all-sky cameras. On the other hand, the
350 presence of aerosols even under cloudy scenes, introduces an additional uncertainty which is
351 difficult to investigate accurately.



353 **Figure 4.** Difference between the estimated using BRL and actual diffuse the diffuse fraction
354 estimated by the ground-based measurements as function of AOD_{500} and FMF_{500}

356 3.2 Sensitivity analysis of the BRL performance under cloud-free sky conditions from RT
357 simulations

358 The uncertainties in estimating diffuse fraction under cloud-free sky conditions, as discussed in
359 section 3.1, are further investigated. We performed RT simulations using libRadtran to calculate GHI
360 and DHI under various aerosol scenarios. The resulting GHI values were then used as input to BRL to
361 estimate the diffuse fraction, which was subsequently compared to the diffuse fraction derived
362 directly from the ratio of DHI to GHI computed by libRadtran.

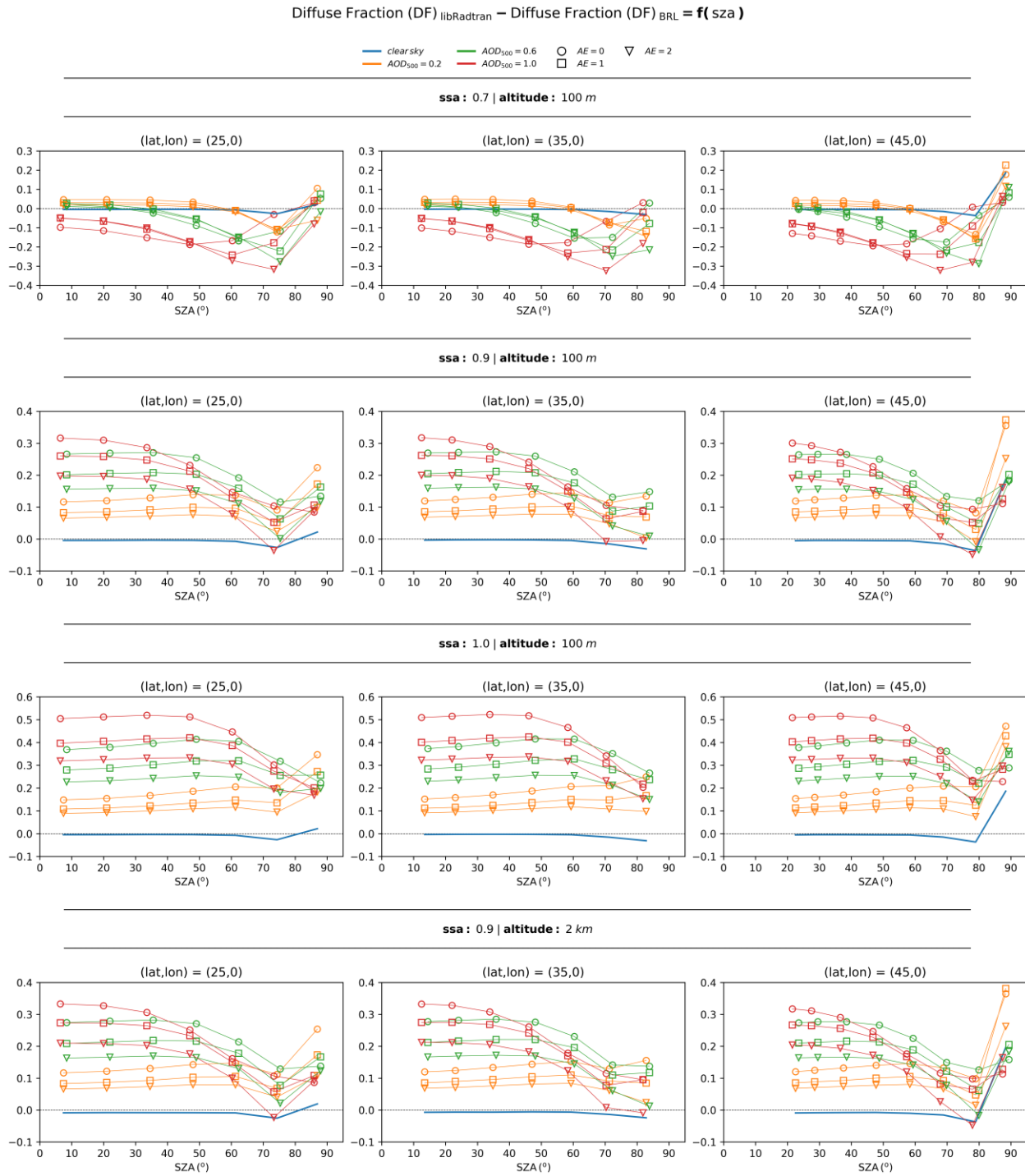
363 To ensure a comprehensive analysis, we considered three representative latitudes (25°, 35° and 45°).
364 Since BRL requires an hourly time-series of GHI as input, the analysis was conducted for the summer
365 solstice. On this day, a sufficient number of hourly values are available, corresponding to a wide
366 range of SZA values, allowing for a robust assessment of the methodology. The sensitivity analysis
367 was performed for surface albedo values of 0.2 and 0.8 as well as for altitudes of 0, 1 and 2 km. For
368 aerosol parameterization, we examined completely clear-sky conditions as a reference, alongside
369 scenarios with AOD_{500} values of 0.2, 0.6, and 1, while varying the SSA and AE. Specifically, the
370 scenarios included SSA values of 0.7, 0.9 and 1, combined with AE values of 0, 1 and 2. The results
371 of this sensitivity analysis for an albedo of 0.2 are provided in Figure 5, while the results for an albedo
372 of 0.8 are included in the supplement (Figure S1).

373 The results confirm that BRL performs well under clear sky conditions and for SZA below 60°, while
374 the incorporation of aerosols in the sky scene introduces larger uncertainties. In all scenarios, we
375 observe that lower values of AE correspond to higher uncertainties. Moreover, ~~regarding SSA~~, when
376 SSA is 0.9 or 1 BRL gradually tends to underestimate the diffuse fraction as aerosol load increases.
377 Instead, when SSA is 0.7, BRL exhibits a different behavior, shifting toward an overestimation of the
378 diffuse fraction at high aerosol loads.

379 The findings of this sensitivity analysis are consistent with the evaluated BRL performance from
380 ground-based measurements presented in section 3.1, especially at SZA smaller than 60° - 70°, and
381 underscore the role of aerosol in the accuracy of diffuse fraction estimations. Differences between
382 the results shown in Figures 2 and 5 at SZA between 60° - 80° can be due to a number of site-related
383 reasons. For example, enhancement of the diffuse component due to scattering by underlying
384 atmospheric layers and clouds in the case of Izaña may compensate the observed overestimation of
385 the diffuse fraction by BRL. Concerning the impact related to AE and SSA, we confirm that the higher

386 underestimations observed for Tamanrasset and Izaña are associated with the optical properties of
387 desert dust aerosol particles. While AE and SSA alone are not sufficient to fully characterize the
388 aerosol type, they serve as strong indicators, aligning with the classification framework of Dubovik et
389 al. (2002). The same comparison for albedo 0.8 (Figure S1 in the supplement) reveals a significant
390 broadening of the discrepancies. Moreover, we observe the presence of a systematic error, even
391 under clear sky conditions.

392 The resulting differences were practically identical across the three selected latitudes, indicating
393 that the BRL model is largely independent of latitude and can therefore be considered as a reliable
394 solution over a wide range of latitudes. Furthermore, the effect of altitude was found to be small.
395 Finally, the outcomes of this analysis highlight potential inconsistencies arising from aerosols with
396 different optical properties. Although the updated parameters of the BRL's model (as implemented
397 in the GSEE model) reported by Lauret et al. (2013) were derived using data from nine worldwide
398 locations, encompassing a broad range of sky conditions that capture a fully representative set of
399 optical properties remain challenging.

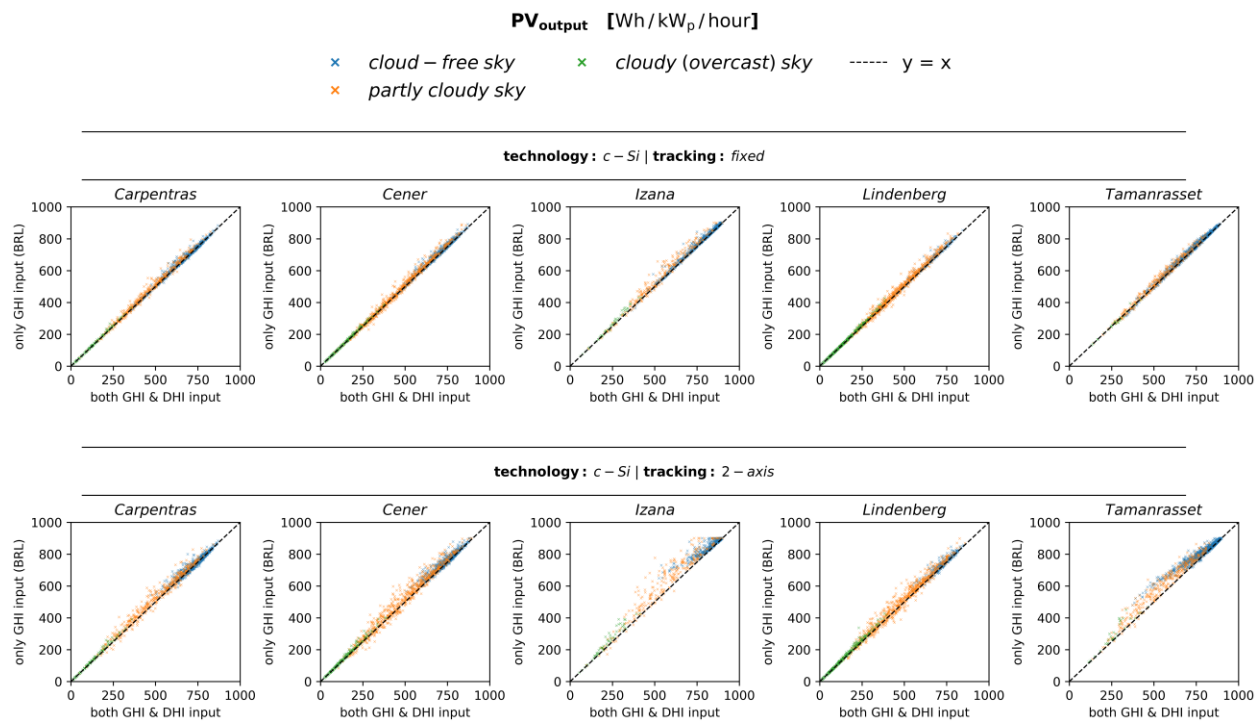


405 3.3 Analysis of the differences in energy production using hourly integrals within the modelling of PV
406 plants

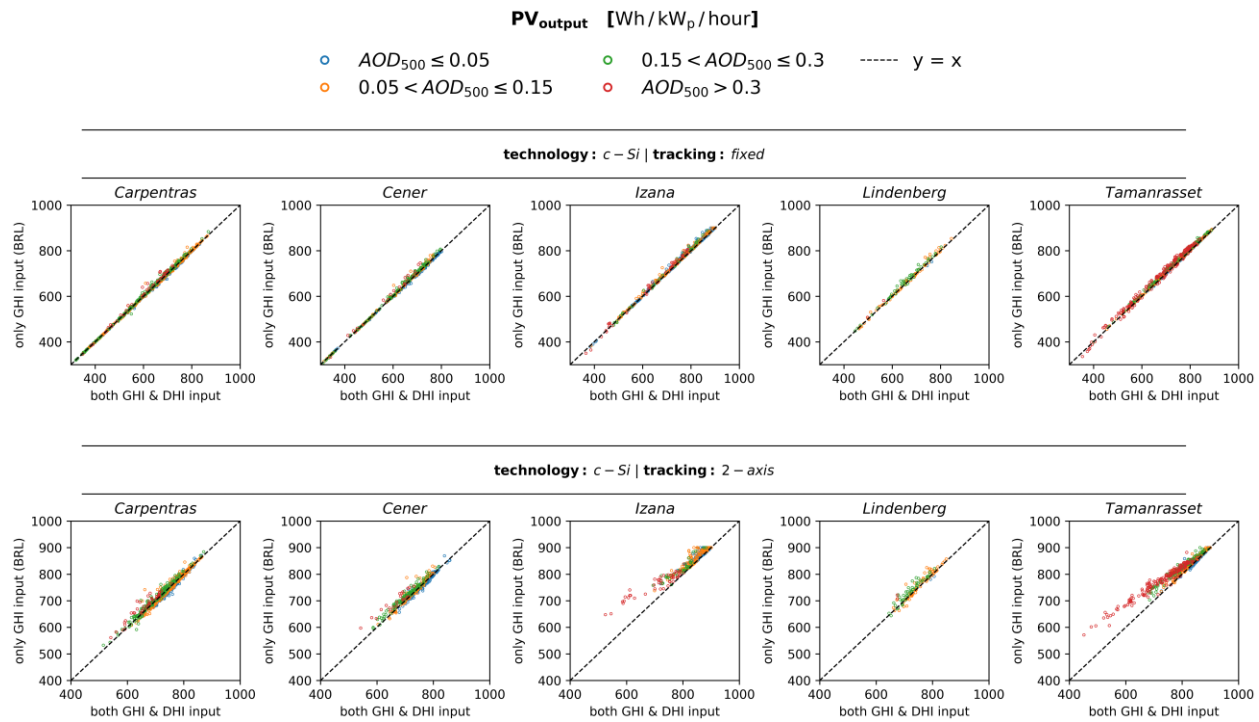
407 Uncertainties in estimating the diffuse fraction influence the calculation of the total irradiance
408 received by an inclined panel's surface, thereby affecting the accuracy of the PV power simulations.
409 In this section, we employ the main submodule of GSEE, used for modelling the electric output from
410 a PV panel, aiming to assess the extent to which these uncertainties propagate to the estimation of
411 the hourly power production. We analyze discrepancies arising from using only GHI from BSRN as
412 input radiation data to the model, instead of both DHI and GHI. More specifically, we compare the
413 total energy produced per hour per unit, expressed in watt-hours (Wh), per unit of nominal power
414 (kWp). The energy production is evaluated for both fixed panels and 2-axis tracking systems.

415 The results of this comparison for c-Si based technology PV panels for different atmospheric
416 conditions are presented in Figure 6, illustrating the impact of cloudiness, and in Figure 7,
417 demonstrating the effect of aerosols. The corresponding results for CdTe technology are provided in
418 the supplement (Figures S2 and S3 respectively). In the modelling of 2-axis solar tracking systems,
419 where the panel is continuously adjusted to maintain a perpendicular orientation to incoming solar
420 radiation, the system becomes more sensitive to uncertainties in the estimation of the diffuse
421 fraction, leading to more significant differences in energy production. Specifically, the contribution
422 of the direct irradiance is maximized in such systems, as the panel exploits the entirety of the
423 available direct irradiance. On the other hand, in the simulation of static panels, the contributions of
424 direct and diffuse components are more evenly distributed, making the impact of diffuse fraction
425 uncertainties less pronounced in energy production.

426 Regarding the uncertainties related to the atmospheric conditions, from Figure 6 we confirm that the
427 highest dispersion occurs in partly cloudy conditions, while from Figure 7, where we examine cloud-
428 free conditions, we note that further improvement achieved as aerosol load decreases. Under totally
429 overcast skies the energy production is extremely low, rendering errors practically negligible.
430 Moreover, accuracy is influenced by aerosols, where a gradual decline in accuracy is detected as
431 aerosol load increases. However, assessing the extent of aerosol loading impact is complex,
432 depending on the interaction of solar radiation with particles of varying optical properties, as
433 extensively analyzed in the previous sections. This effect becomes particularly evident in cases of
434 high aerosol loading, where a noticeable offset is observed, while under certain conditions, the
435 associated uncertainty is comparable to that found in partly cloudy conditions.



437 **Figure 6.** Comparison of the estimated hourly PV power generation between simulations performed
 438 using GSEE with input data consisting of either only GHI or both GHI and DHI under varying
 439 cloudiness conditions: (top) fixed panels (bottom) 2-axis tracking systems



441 **Figure 7.** Comparison of the estimated hourly PV power generation between simulations performed
 442 using GSEE with input data consisting of either only GHI or both GHI and DHI under varying aerosol
 443 conditions: (top) fixed panels (bottom) 2-axis tracking systems

444 The PV systems considered in this study have a nominal capacity of 1 kWp. The PV model applies a
 445 default system loss factor of 10%. This effectively limits the maximum achievable power output to
 446 approximately 90% of the nominal capacity (i.e., around 900 W/kWp). This effect becomes apparent
 447 at the Izaña site due to its low latitude combined with its specific geographical and atmospheric
 448 conditions, which lead to high irradiance levels. As a result, the simulated PV output in some cases
 449 appears capped around 900 Wh/kWp per hour when only GHI is used.

450 Additionally, Tables S1-S5 in the supplement⁴ and 5 present the validation results, including
 451 computed for Carpentras and Tamanrasset, selected as representative locations that encompass a
 452 wide variety of sky conditions. Validation results for the remaining stations are available in the
 453 supplement (Tables S1-S3). All the evaluation metrics that quantify the errors. All the computations
 454 correspond to simulations of PV panels with c-Si technology.

455 **Table 4.** Evaluation metrics for GSEE performance within hourly intervals in Carpentras, comparing
 456 simulations with diffuse fraction from measurements and from the BRL model

STATION: Carpentras		fixed panels			2-axis tracking		
		RMSE (Wh/kWp/hour)	MAE (Wh/kWp/hour)	rMBE (%)	RMSE (Wh/kWp/hour)	MAE (Wh/kWp/hour)	rMBE (%)
All-Sky scenes		12.6	6.6	0.8	20.8	12.5	1.2
All-Sky scenes (cloudiness)	cloud-free	9.2	4.6	0.4	14.8	8.7	0.5
	partly cloudy	19.5	12.5	2.3	32.5	23.9	3.8
	cloudy (overcast)	5.8	3.0	2.0	10.5	6.1	4.6
Cloudless- Sky scenes (aerosol load)	low	4.7	3.4	-0.4	9.5	7.5	-0.8
	moderate	4.3	2.2	0.1	7.8	4.7	0.0
	high	6.4	4.0	0.6	11.0	7.8	0.9
	very high	14.9	10.2	1.6	22.7	17.2	2.6

457

458 **Table 5.** Evaluation metrics for GSEE performance within hourly intervals in Tamanrasset,
 459 comparing simulations with diffuse fraction from measurements and from the BRL model.

STATION: Tamanrasset		fixed panels			2-axis tracking		
		RMSE (Wh/kWp/hour)	MAE (Wh/kWp/hour)	rMBE (%)	RMSE (Wh/kWp/hour)	MAE (Wh/kWp/hour)	rMBE (%)

All-Sky scenes		13.6	9.3	1.0	40.4	27.8	3.8
All-Sky scenes (cloudiness)	cloud-free	11.5	8.0	0.8	35.3	23.4	2.9
	partly cloudy	20.1	15.0	2.0	56.1	45.7	8.1
	cloudy (overcast)	8.4	5.2	-0.1	45.3	30.1	11.2
Cloudless- Sky scenes (aerosol load)	low	3.2	2.0	0.2	6.6	4.0	0.3
	moderate	5.4	4.6	0.6	13.0	10.5	1.2
	high	12.5	11.7	1.6	30.1	27.4	3.4
	very high	18.0	16.2	1.9	57.0	49.2	6.8

460

461 Based on the calculated statistical indices, the Root Mean Square Error (RMSE) values for fixed
 462 panels range from 4.7 Wh/kWp/hour (clear sky) to 19.5 Wh/kWp/hour (partly cloudy) in Carpentras,
 463 and from 3.2 to 20.1 Wh/kWp/hour in Tamanrasset. Under very high aerosol loading, RMSE reaches
 464 14.9 and 18.0 Wh/kWp/hour, respectively. For 2-axis tracking systems, RMSE values vary
 465 significantly, ranging from 9.5 to 32.5 Wh/kWp/hour in Carpentras and from 6.6 to 56.1 Wh/kWp/hour
 466 in Tamanrasset, with peaks of 22.7 and 57.0 Wh/kWp/hour under very high aerosol loading
 467 conditions. Similarly, the Mean Absolut Error (MAE) values are generally lower for fixed panels (3.4-
 468 12.5 Wh/kWp//hour in Carpentras, 2.0-15.0 in Tamanrasset) and substantially higher for 2-axis
 469 tracking (7.5-23.9 and 4.0-45.7 Wh/kWp/hour, respectively). Notably in Tamanrasset, MAE values
 470 under very high aerosol loading exceed those observed under partly cloudy conditions, with values
 471 increasing from 15.0 to 16.2 Wh/kWp/hour for fixed panels and from 45.7 to 49.2 Wh/kWp/hour for
 472 2-axis tracking systems. Regarding the relative mean bias (rMBE), this remains mostly within $\pm 4.6\%$
 473 for fixed panels but can reach up to 11.2% for 2-axis tracking, particularly in aerosol-laden
 474 conditions.

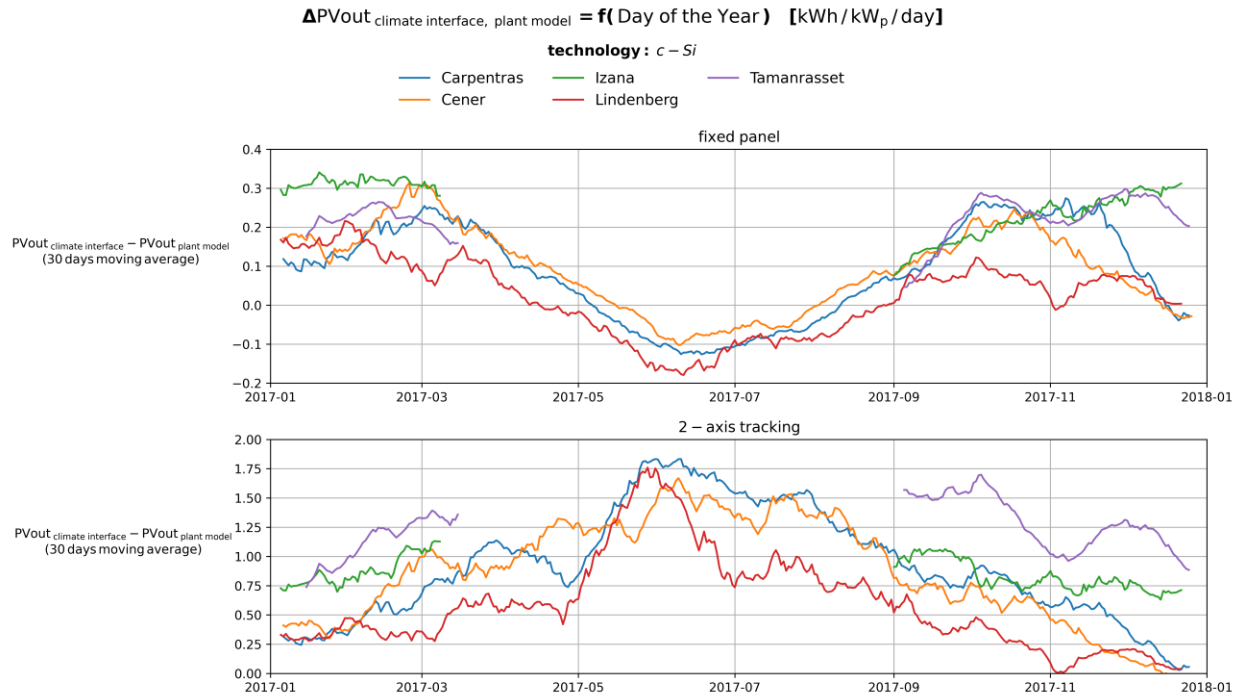
475

476 3.4 Estimating total daily PV power output using the Climate Interface

477 Validation of the estimated daily energy production using the Climate Interface is achieved by
 478 comparing the estimates with the results obtained from the direct summation of the hourly
 479 simulations with input both GHI and DHI.

480 The Climate Interface generates the hourly profile of GHI for each day as a sinusoidal function. Then,
 481 the BRL is applied to the hourly time-series, and the hourly power generation is computed. Finally,
 482 these values are summed up to provide an estimate of the total daily output power. As shown in
 483 Figure Fig. 8, which illustrates the differences between the Climate Interface estimates and the sums

484 of the hourly simulations, this approach introduces a variability throughout the year. Furthermore,
 485 Figure S6 in the supplement presents the percentage differences between the two approaches, using
 486 the latter as the reference.



487

488 **Figure 8.** Time-series of the differences between the daily PV output estimated using the climate
 489 interface and the corresponding daily sums from hourly simulations.

490

491 The time-series represent the centered 30-day moving average. To ensure that the values are
 492 representative of the reference period, we have applied all conditions requiring at least 20 days of
 493 available data within each 30-days interval. In Tamanrasset and Izaña, especially during the summer
 494 months, there are significant data gaps on several days, often occurring around solar noon.

495 More precisely, from Figure Fig. 8, we observe that within the modelling of PV plants with fixed panels,
 496 there is a tendency to overestimate in winter, with deviations of approximately 0.3 kWh/kWp/day, and
 497 to slightly underestimate in summer, where deviations are around 0.1 kWh/kWp/day. In contrast, for
 498 2-axis solar tracking systems, the resulting deviations are significantly larger, with a general tendency
 499 toward overestimation that peaks during summer, reaching approximately 1.75 kWh/kWp/day. The

500 [percentage differences span from -10 to 20 % for fixed panels and from -5 to 35 % for 2-axis tracking](#)
501 [systems.](#)

502 The variability in the percentage difference between the daily PV output estimated using the climate
503 interface and the corresponding daily sums is mainly a function of the minimum SZA, while
504 especially in the case of modeling for 2-axes tracking systems, the variation is also influenced by
505 aerosol loading, with differences tending to increase as aerosol load rises (Figures S4 and S5 in the
506 supplement).

507 Additional validation results are provided in the supplement (Tables [S6-S10](#)). Indicatively, for
508 [Carpentras and Tamanrasset, representative results are discussed below. For fixed panels, RMSE is](#)
509 [minimized at 0.18 kWh/kWp/day under very-low aerosol conditions, compared to the overall 0.22](#)
510 [kWh/kWp/day for Carpentras. In Tamanrasset, the lowest RMSE is observed at 0.15 kWh/kWp/day](#)
511 [under very low aerosol conditions, while the overall reaches 0.24. In the case of 2-axis tracking, a](#)
512 [significant increase is observed from low-aerosol to aerosol-laden conditions, ranging from 0.82 to](#)
513 [1.28 kWh/kWp/day in Carpentras and from 0.66 to 1.37 in Tamanrasset. Similar widening trends are](#)
514 [also evident in the MAE values across different aerosol loading conditions.](#) The computed statistical
515 indices confirm that the differences are minimized under sunny and nearly aerosol-free sky
516 conditions. Comparing the performance on low-aerosol days to that on aerosol-laden, we conclude
517 that, particularly in the case of modelling 2-axis tracking systems, errors increase significantly. In
518 Tamanrasset, in particular, the errors are more than double.

519 [3.5 Evaluation of the reliability of using the CAMS solar radiation time-series product in modelling](#)
520 [PV power potential](#)

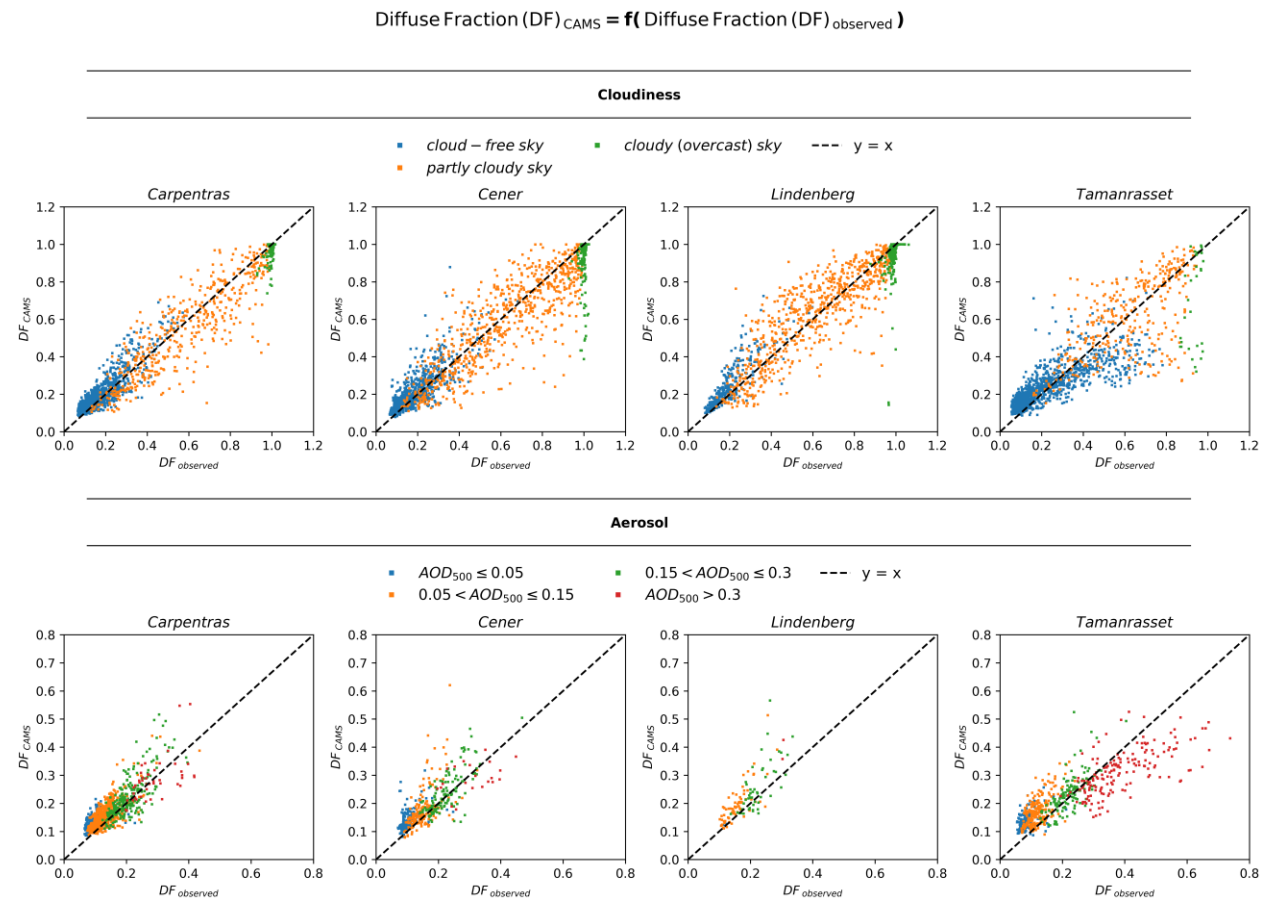
521 The aim of this section is to inspect the reliability of using the CAMS solar radiation time-series
522 product in modelling the PV power potential adapted to a certain location;. [A review of the existing](#)
523 [literature indicates a lack of studies directly examining the accuracy of using CAMS data for](#)
524 [assessing PV power potential. This is addressed](#) by comparing the output power obtained from using
525 CAMS solar radiation data with that calculated using ground-based measurements. The analysis
526 focuses on the capability of CAMS to provide accurate estimates of both GHI as well as its individual
527 components.

528 In this section, we have excluded Izaña, because, due to its high altitude – as indicated through a
529 personal communication with Yves-Marie Saint-Drenan (2025) – comparable results would require

530 adjusting the measurements to the elevation of the stations, which is a complicated process and
531 beyond the scope of this study.

532 The CAMS-based diffuse fraction, compared to the observed, is presented in Figure 9 under different
533 prevailing conditions. We observe that the calculation of the diffuse component is subject to
534 significant uncertainty. Cloudiness is the primary uncertainty source, particularly under partly cloudy
535 conditions. Additionally, notable discrepancies related to aerosols emerge only in cases of very high
536 aerosol loading.

537



538

539 **Figure 9.** Comparison of the CAMS-based diffuse fraction estimated using BRL with the actual one
540 under diverse atmospheric conditions

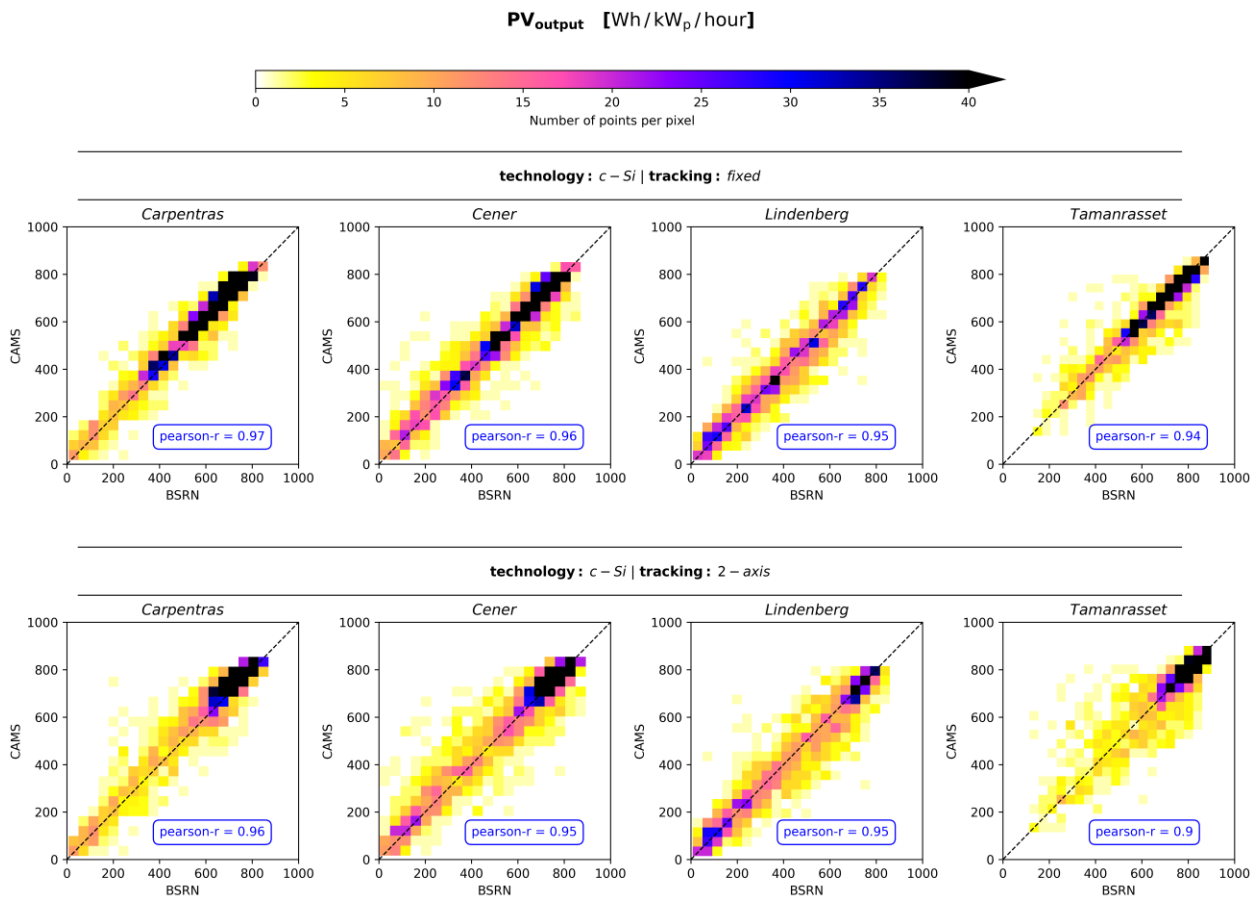
541

542 In [Figure Fig.](#) 10 we provide density scatter plots comparing the CAMS-based PV output power with
543 that computed from the ground-based BSRN data, aiming to illustrate how the uncertainty in the

544 diffuse component estimates propagate to the calculation of power generation. Notably, there is a
545 much greater dispersion from the $y=x$ line in the case of simulating PV plants with 2-axis tracking
546 system, compared to that within the modelling of fixed panels. This outcome is attributed to the
547 increased sensitivity of the 2-axis tracking systems to the partitioning of global irradiance into its
548 components. Nevertheless, correlation coefficients are in all cases better than 0.9. ~~Additional
549 evaluation metrics are provided in the supplement (Tables S11-S14).~~

550 ~~Additional evaluation metrics are provided in the supplement (Tables S9-S12). Indicatively, we
551 observe that under cloudless conditions, for fixed panels, RMSE ranges between 25.0 to 42.3
552 Wh/kWp/hour in Carpentras and 16.6 and 31.0 Wh/kWp/hour in Tamanrasset, with variations linked
553 to aerosol loading. Similarly, MAE ranges from 20.0 to 36.9 Wh/kWp/hour in Carpentras and 11.9 to
554 22.9 Wh/kWp/hour in Tamanrasset. For 2-axis systems, RMSE and MAE follow similar trend, ranging
555 from 28.8 to 49.9 Wh/kWp/hour and 22.3 to 44.1 Wh/kWp/hour, respectively, in Carpentras, and from
556 20.8 to 48.0 Wh/kWp/hour and 15.3 to 35.5 Wh/kWp/hour, respectively, in Tamanrasset. Conversely,
557 under cloudy conditions the errors are significantly increasing. In Carpentras, as well as in Cener,
558 and Lindenberg (according to the corresponding tables in the supplement) the errors peak under
559 partly cloudy conditions, with RMSE reaching up to 94.2 Wh/kWp/hour in Carpentras. However, in
560 Tamanrasset, the highest errors occur under overcast conditions, where RMSE and MAE for 2-axis
561 solar tracking systems reach 210.7 and 151.6 Wh/kWp/hour, respectively. This exception can be
562 interpreted through Figure 15, which illustrates that in the rare overcast scenes in Tamanrasset,
563 CAMS occasionally reports low diffuse fraction values instead of values close to 1, suggesting that
564 CAMS did not accurately represent cloudiness in these cases.~~

565



569 4. Conclusions

570 ~~This study evaluated different solar radiation information that is commonly used for PV power~~
 571 ~~modelling, and their implications for PV modelling accuracy. The optimal approach to include solar~~
 572 ~~radiation information to PV power models such as GSEE is to use actual in-situ measurements of~~
 573 ~~global and diffuse solar irradiance. Since measurements of the diffuse component are rarely~~
 574 ~~available, it is common to use measurements of the GHI (if available) and retrieve the diffuse~~
 575 ~~component using a model such as BRL. In the absence of in-situ measurements, other options~~
 576 ~~include the use of datasets such as CAMS or even a radiative transfer model, provided that~~
 577 ~~atmospheric inputs such as clearness index, aerosol optical depth (AOD), and other aerosol~~
 578 ~~properties are available. This study evaluated these options and their implications for PV modelling~~
 579 ~~accuracy.~~

580 The results highlighted the importance of having precise information for the distribution of solar
581 irradiance among its components in PV power modelling. The implementation of the BRL diffuse
582 fraction within GSEE serves as a practical, and under certain conditions, reliable solution to the
583 absence of detailed information for each component separately. Moreover, the integrated Climate
584 Data Interface submodule offers valuable prospects for investigating fluctuations in the solar PV
585 power generation across various timescales. In this context, the use of BRL has a key contribution
586 alongside the other computational procedures in processing climate datasets. Previous studies on
587 PV power modelling approaches have not examined their reliability under diverse atmospheric
588 conditions, including the effects associated with cloudiness, aerosol loading, as well as aerosol
589 optical properties.

590 The evaluation of the BRL's performance revealed a dependency of its reliability on the prevailing sky
591 conditions. ~~As a result, discrepancies arising from inconsistencies in diffuse fraction estimation~~
592 ~~propagate to PV power generation. Within the modelling of PV plants equipped with 2-axis solar~~
593 ~~tracking system, the deviations are much more pronounced relative to optimally inclined panels.~~ BRL
594 has excellent accuracy under totally clear sky scenes and still performs well for cloudless scenes
595 with moderate aerosol loading. In general, its accuracy is inversely proportional to the complexity of
596 the cloud scene. However, the model systematically underestimates the diffuse fraction under high-
597 loading conditions, such as during dust events. ~~Under such circumstances, this bias can potentially~~
598 ~~lead to significant overestimation of power generation by up to 49.2 Wh/kWp/hour~~ The discrepancies
599 ~~arising from diffuse fraction estimation propagate to PV power generation and become particularly~~
600 ~~pronounced in the modelling of 2-axis tracking systems. Indicatively, MAE under cloud-free scenes~~
601 ~~with moderate aerosol loading, ranges between 2.2 to 6.6 Wh/kWp/hour for fixed panels and 4.7 to~~
602 ~~15.0 Wh/kWp/hour for 2-axis tracking systems. Under partly cloudy conditions, where the cloud~~
603 ~~scene is more complex, the MAE increases substantially, ranging from 12.4 to 25.8 Wh/kWp/hour for~~
604 ~~fixed panels and from 23.5 to 55.1 Wh/kWp/hour for 2-axis tracking systems. Moreover, during~~
605 ~~intense dust events, MAE can reach up to 49.2 Wh/kWp/hour in Tamanrasset, which is comparable~~
606 ~~to that computed under partly cloudy conditions. Overall, the rMBE remains within the +5%, with the~~
607 ~~exception of a limited cases under overcast conditions. The same analysis applied to CdTe panels~~
608 ~~yielded similar results, with minor differences.~~

609 Aiming to provide an indicative assessment of the financial impacts of the effect of desert dust
610 aerosols, we assume that the statistical indices calculated for Tamanrasset are representative of a

611 large-scale solar farm located in the Sahara region, with 500 MW installed PV capacity and systems
612 equipped with 2-axis solar tracking system. For this hypothetical solar farm, according to the value
613 of the Mean Absolute Error (MAE) on Table 4 for very high aerosol loading, we estimate that the
614 produced energy is $0.0492 [kWh/kWp/hour] \times 500 \times 10^3 [kWp] = 24600 [kWh/hour]$
615 *supposing 12 sunlight hours per day* $\rightarrow \sim 295200 [kWh/day]$ less than the expected from the PV power
616 simulations. According to the global average auction prices for selling produced energy back to the
617 grid in 2021 (IRENA, n.d.), the overestimations are equivalent to a financial loss of
618 $0.039 [USD/kWh] \times 295200 [kWh/day] \approx 11,500 USD/day$. Therefore, site assessments that do
619 not correctly account for the impactdistribution of surface solar irradiance in the sky under desert
620 dust aerosolsaerosol conditions may overestimate financial performance and the annual financial
621 deficit could be accumulated to hundreds of thousands of US dollars per year.

622 Comparing the range of computed errors, we observe that the errors arising from employing CAMS
623 rather than using ground-based measurements, even when the diffuse fraction is not provided, are
624 higher across the overwhelming majority of the considered sky conditions. More specifically,
625 regarding the overall performance, MAE when using CAMS ranges between 33.7 and 46.1
626 Wh/kWp/hour, while with ground-based GHI measurements, MAE remains below 10 Wh/kWp/hour
627 within the modelling of systems with fixed panels and can reach up to 27.8 Wh/kWp/hour within the
628 modelling of 2-axis tracking systems. This outcome highlights the value of ground-based
629 measurements.

630 To sum up, achieving the highest quality PV power simulations necessitates high-quality, concurrent
631 measurements of solar irradiance components. In absence of this, the submodules included in the
632 GSEE package enable reliable simulations under the vast majority of prevailing sky conditions. CAMS
633 serves as a valuable data source for PV power modelling, but it cannot fully replace the precision and
634 reliability of using ground-based measurements. The integration of aerosol correction within the BRL
635 model opens new possibilities for further improvements in the modelling of solar energy systems. A
636 more comprehensive assessment would require measured PV output data; however, acquiring
637 simultaneous direct and diffuse irradiance measurements at the same location as the solar farms
638 remains challenging.

639

640 **Data availability**

641 The BSRN data are freely available on the BSRN web-page (<https://bsrn.awi.de/>). The AERONET
642 version 3 products are freely available from the AERONET website (<https://aeronet.gsfc.nasa.gov/>).
643 The CAMS radiation time-series are available from the Atmosphere Data Store
644 (<https://ads.atmosphere.copernicus.eu>). The rest of the data used in this paper are available upon
645 request from the authors.

646 **Author Contributions**

647 Conceptualization: NP and IF; Data curation: NP and KP; Formal analysis: NP; Funding acquisition:
648 CZ; Investigation: NP; Methodology: NP, IF, SK, AK and AG; Project administration: CZ; Resources: SP,
649 KP and LD; Software: NP; Supervision: IF; Validation: NP, IF and SP; Visualization: NP; Writing –
650 original draft: NP; Writing – review & editing: all authors

651 **Funding**

652 This work has been supported by the action titled “Support for upgrading the operation of the
653 National Network for Climate Change (CLIMPACT II)”, funded by the Public Investment Program of
654 Greece, General Secretary of Research and Technology/Ministry of Development and Investments.
655 Part of this work was also supported by the COST Action Harmonia (CA21119) supported by COST
656 (European Cooperation in Science and Technology). This work was partially funded by the
657 Copernicus Climate Change Service under contracts C3S2 _461-1_GR (Seasonal to decadal
658 predictions for national renewable energy management).

659 **Acknowledgments**

660 We thank the teams of the AERONET for ground measurements and maintenance, and CAMS for the
661 data production and distribution. We would like to thank the five site instrument operators and
662 technical staff of the BSRN network stations who made the ground-based measurements feasible.
663 A. Gkikas, J. Kapsomenakis, and C.S. Zerefos also acknowledge “CAMS2_82 Project: Evaluation and
664 Quality Control (EQC) of global products.”

665 **References**

666 Anderson, G., Clough, S., Kneizys, F., Chetwynd, J., & Shettle, E. (1986). *AFGL atmospheric*
667 *constituent profiles (0-120 km)* (Tech. Rep. AFGL-TR-86-0110). Air Force Geophysics Laboratory,
668 Hanscom Air Force Base.

669 Anderson, K. S., Hansen, C. W., Holmgren, W. F., Jensen, A. R., Mikofski, M. A., & Driesse, A.
670 (2023). *pvlib python: 2023 project update*. *Journal of Open Source Software*, 8(92), Article 5994.
671 <https://doi.org/10.21105/joss.05994>

672 Ångström, A. (1929). On the atmospheric transmission of sun radiation and on dust in the
673 air. *Geografiska Annaler*, 11(2), 156–166. <https://doi.org/10.1080/20014422.1929.11880498>

674 Barreto, Á., García, R. D., Guirado-Fuentes, C., Cuevas, E., Almansa, A. F., Milford, C., Toledano,
675 C., Expósito, F. J., Díaz, J. P., & León-Luis, S. F. (2022). Aerosol characterisation in the
676 subtropical eastern North Atlantic region using long-term AERONET
677 measurements. *Atmospheric Chemistry and Physics*, 22(17), 11105–11124.
678 <https://doi.org/10.5194/acp-22-11105-2022>

679 Blaga, R., Mares, O., Paulescu, E., Boata, R., Sabadus, A., Hategan, S.-M., Calinou, D., Stefu,
680 N., & Paulescu, M. (2024). Diffuse fraction as a tool for exploring the sensitivity of parametric
681 clear-sky models to changing aerosol conditions. *Solar Energy (Phoenix, Ariz.)*, 277(112731),
682 112731. <https://doi.org/10.1016/j.solener.2024.112731>

683 Blanc, P., Remund, J., & Vallance, L. (2017). Short-term solar power forecasting based on
684 satellite images. In *Renewable Energy Forecasting* (pp. 179–198). Elsevier.

685 Boland, J. W., Scott, L., & Luther, M. (2001). *Modelling the diffuse fraction of global solar*
686 *radiation on a horizontal surface*. *Environmetrics*, 12(2), 103–116. [https://doi.org/10.1002/1099-095X\(200103\)12:2<103::AID-ENV447>3.0.CO;2-2](https://doi.org/10.1002/1099-095X(200103)12:2<103::AID-ENV447>3.0.CO;2-2)

688 Buras, R., Dowling, T., & Emde, C. (2011). New secondary-scattering correction in DISORT with
689 increased efficiency for forward scattering. *Journal of Quantitative Spectroscopy & Radiative*
690 *Transfer*, 112(12), 2028–2034. <https://doi.org/10.1016/j.jqsrt.2011.03.019>

691 Cañadillas-Ramallo, D., Moutaoikil, A., Shephard, L. E., & Guerrero-Lemus, R. (2022). The
692 influence of extreme dust events in the current and future 100% renewable power scenarios in
693 Tenerife. *Renewable Energy*, 184, 948–959. <https://doi.org/10.1016/j.renene.2021.12.013>

694 Copernicus Atmosphere Monitoring Service. (2020). *CAMS solar radiation time-series*.
695 Copernicus Atmosphere Monitoring Service (CAMS) Atmosphere Data Store.
696 <https://doi.org/10.24381/5cab0912>

697 Cuevas, E., Romero-Campos, P. M., Kouremeti, N., Kazadzis, S., Räisänen, P., García, R. D.,
698 Barreto, A., Guirado-Fuentes, C., Ramos, R., Toledano, C., Almansa, F., & Gröbner, J. (2019).
699 Aerosol optical depth comparison between GAW-PFR and AERONET-Cimel radiometers from
700 long-term (2005–2015) 1 min synchronous measurements. *Atmospheric Measurement
701 Techniques*, 12(8), 4309–4337. <https://doi.org/10.5194/amt-12-4309-2019>

702 Driemel, A., Augustine, J., Behrens, K., Colle, S., Cox, C., Cuevas-Agulló, E., Denn, F. M., Duprat,
703 T., Fukuda, M., Grobe, H., Haeffelin, M., Hodges, G., Hyett, N., Ijima, O., Kallis, A., Knap, W.,
704 Kustov, V., Long, C. N., Longenecker, D., ... König-Langlo, G. (2018). Baseline Surface Radiation
705 Network (BSRN): structure and data description (1992–2017). *Earth System Science
706 Data*, 10(3), 1491–1501. <https://doi.org/10.5194/essd-10-1491-2018>

707 Dubey, S., Sarvaiya, J. N., & Seshadri, B. (2013). Temperature dependent photovoltaic (PV)
708 efficiency and its effect on PV production in the world – A review. *Energy Procedia*, 33, 311–321.
709 <https://doi.org/10.1016/j.egypro.2013.05.072>

710 Dubovik, O., Holben, B., Eck, T. F., Smirnov, A., Kaufman, Y. J., King, M. D., Tanré, D., & Slutsker, I.
711 (2002). Variability of absorption and optical properties of key aerosol types observed in
712 worldwide locations. *Journal of the Atmospheric Sciences*, 59(3), 590–608.
713 [https://doi.org/10.1175/1520-0469\(2002\)059<0590:voaaop>2.0.co;2](https://doi.org/10.1175/1520-0469(2002)059<0590:voaaop>2.0.co;2)

714 Dubovik, O., & King, M. D. (2000). A flexible inversion algorithm for retrieval of aerosol optical
715 properties from Sun and sky radiance measurements. *Journal of Geophysical
716 Research*, 105(D16), 20673–20696. <https://doi.org/10.1029/2000jd900282>

717 Edenhofer, O., Pichs-Madruga, R., Sokona, Y., Seyboth, K., Kadner, S., Zwickel, T., Eickemeier, P.,
718 Hansen, G., Schlomer, S., & Von Stechow, C. (Eds.). (2011). *Renewable energy sources and
719 climate change mitigation: Special report of the intergovernmental panel on climate change*.
720 Cambridge University Press.

721 Emde, C., Buras-Schnell, R., Kylling, A., Mayer, B., Gasteiger, J., Hamann, U., Kylling, J., Richter,
722 B., Pause, C., Dowling, T., & Bugliaro, L. (2016). The libRadtran software package for radiative
723 transfer calculations (version 2.0.1). *Geoscientific Model Development*, 9(5), 1647–1672.
724 <https://doi.org/10.5194/gmd-9-1647-2016>

725 Faid, A., Smara, Y., Caselles, V., & Khireddine, A. (2012). Evaluation of the Saharan aerosol
726 impact on solar radiation over the Tamanrasset area, Algeria. *International Journal of Advanced*
727 *Research in Engineering and Technology*, 3(1), 24–32.

728 Fountoulakis, I., Kosmopoulos, P., Papachristopoulou, K., Raptis, I.-P., Mamouri, R.-E., Nisantzi,
729 A., Gkikas, A., Witthuhn, J., Bley, S., Moustaka, A., Buehl, J., Seifert, P., Hadjimitsis, D. G.,
730 Kontoes, C., & Kazadzis, S. (2021). Effects of aerosols and clouds on the levels of surface solar
731 radiation and solar energy in Cyprus. *Remote Sensing*, 13(12), 2319.
732 <https://doi.org/10.3390/rs13122319>

733 Fountoulakis, I., Papachristopoulou, K., Proestakis, E., Amiridis, V., Kontoes, C., & Kazadzis, S.
734 (2022). Effect of aerosol vertical distribution on the modeling of solar radiation. *Remote*
735 *Sensing*, 14(5), 1143. <https://doi.org/10.3390/rs14051143>

736 Giles, D. M., Sinyuk, A., Sorokin, M. G., Schafer, J. S., Smirnov, A., Slutsker, I., Eck, T. F., Holben,
737 B. N., Lewis, J. R., Campbell, J. R., Welton, E. J., Korkin, S. V., & Lyapustin, A. I. (2019).
738 Advancements in the Aerosol Robotic Network (AERONET) Version 3 database – automated
739 near-real-time quality control algorithm with improved cloud screening for Sun photometer
740 aerosol optical depth (AOD) measurements. *Atmospheric Measurement Techniques*, 12(1),
741 169–209. <https://doi.org/10.5194/amt-12-169-2019>

742 Holben, B. N., Eck, T. F., Slutsker, I., Tanré, D., Buis, J. P., Setzer, A., Vermote, E., Reagan, J. A.,
743 Kaufman, Y. J., Nakajima, T., Lavenu, F., Jankowiak, I., & Smirnov, A. (1998). AERONET—A
744 federated instrument network and data archive for aerosol characterization. *Remote Sensing of*
745 *Environment*, 66(1), 1–16. [https://doi.org/10.1016/s0034-4257\(98\)00031-5](https://doi.org/10.1016/s0034-4257(98)00031-5)

746 Hou, X., Wild, M., Folini, D., Kazadzis, S., & Wohland, J. (2021). Climate change impacts on solar
747 power generation and its spatial variability in Europe based on CMIP6. *Earth System*
748 *Dynamics*, 12(4), 1099–1113. <https://doi.org/10.5194/esd-12-1099-2021>

749 Huld, T., Gottschalg, R., Beyer, H. G., & Topič, M. (2010). Mapping the performance of PV
750 modules, effects of module type and data averaging. *Solar Energy (Phoenix, Ariz.)*, 84(2), 324–
751 338. <https://doi.org/10.1016/j.solener.2009.12.002>

752 Intergovernmental Panel on Climate Change (IPCC). (2023). *Climate change 2022 – impacts,
753 adaptation and vulnerability: Working group II contribution to the sixth assessment report of the*

754 *intergovernmental panel on climate change*. Cambridge University Press.

755 <https://doi.org/10.1017/9781009325844>

756 Jacovides, C. P., Tymvios, F. S., Assimakopoulos, V. D., & Kaltsounides, N. A. (2006).

757 Comparative study of various correlations in estimating hourly diffuse fraction of global solar

758 radiation. *Renewable Energy*, 31(15), 2492–2504. <https://doi.org/10.1016/j.renene.2005.11.009>

759 Kakran, S., Rathore, J. S., Sidhu, A., & Kumar, A. (2024). Solar energy advances and CO₂

760 emissions: A comparative review of leading nations' path to sustainable future. *Journal of*

761 *Cleaner Production*, 475(143598), 143598. <https://doi.org/10.1016/j.jclepro.2024.143598>

762 Kato, S., Ackerman, T. P., Mather, J. H., & Clothiaux, E. E. (1999). The k-distribution method and

763 correlated-k approximation for a shortwave radiative transfer model. *Journal of Quantitative*

764 *Spectroscopy & Radiative Transfer*, 62(1), 109–121. [https://doi.org/10.1016/s0022-4073\(98\)00075-2](https://doi.org/10.1016/s0022-4073(98)00075-2)

765

766 Kazantzidis, A., Tzoumanikas, P., Blanc, P., Massip, P., Wilbert, S., & Ramirez-Santigosa, L.

767 (2017). Short-term forecasting based on all-sky cameras. In *Renewable Energy Forecasting* (pp.

768 153–178). Elsevier.

769

770 [Kosmopoulos, P., Kazadzis, S., El-Askary, H., Taylor, M., Gkikas, A., Proestakis, E., Kontoes, C., & El-Khayat, M. \(2018\). Earth-Observation-based estimation and forecasting of particulate matter impact on solar energy in Egypt. *Remote Sensing*, 10\(12\), 1870.](#)

771

772 <https://doi.org/10.3390/rs10121870>

773

774 [Kouklaki, D., Kazadzis, S., Raptis, I.-P., Papachristopoulou, K., Fountoulakis, I., & Eleftheratos, K. \(2023\). Photovoltaic spectral responsivity and efficiency under different aerosol conditions. *Energies*, 16\(18\), 6644. https://doi.org/10.3390/en16186644](#)

775

776

777

778 Lauret, P., Boland, J., & Ridley, B. (2013). Bayesian statistical analysis applied to solar radiation

779 modelling. *Renewable Energy*, 49, 124–127. <https://doi.org/10.1016/j.renene.2012.01.049>

780 Liu, B. Y. H., & Jordan, R. C. (1960). The interrelationship and characteristic distribution of
781 direct, diffuse and total solar radiation. *Solar Energy (Phoenix, Ariz.)*, 4(3), 1–19.
782 [https://doi.org/10.1016/0038-092x\(60\)90062-1](https://doi.org/10.1016/0038-092x(60)90062-1)

783 Logothetis, S.-A., Salamalikis, V., & Kazantidis, A. (2020). Aerosol classification in Europe,
784 Middle East, North Africa and Arabian Peninsula based on AERONET Version 3. *Atmospheric*
785 *Research*, 239(104893), 104893. <https://doi.org/10.1016/j.atmosres.2020.104893>

786 Long, C., & Dutton, E. (2010). *BSRN Global Network recommended QC tests, V2.x*.
787 https://epic.awi.de/id/eprint/30083/1/BSRN_recommended_QC_tests_V2.pdf

788 Mayer, B., & Kylling, A. (2005). Technical note: The libRadtran software package for radiative
789 transfer calculations - description and examples of use. *Atmospheric Chemistry and*
790 *Physics*, 5(7), 1855–1877. <https://doi.org/10.5194/acp-5-1855-2005>

791 McMahan, A. C., Grover, C. N., & Vignola, F. E. (2013). Evaluation of resource risk in solar-
792 project financing. In *Solar Energy Forecasting and Resource Assessment* (pp. 81–95). Elsevier.

793 Owusu, P. A., & Asumadu-Sarkodie, S. (2016). A review of renewable energy sources,
794 sustainability issues and climate change mitigation. *Cogent Engineering*, 3(1), 1167990.
795 <https://doi.org/10.1080/23311916.2016.1167990>

796 Papachristopoulou, K., Fountoulakis, I., Bais, A. F., Psiloglou, B. E., Papadimitriou, N., Raptis, I.-
797 P., Kazantidis, A., Kontoes, C., Hatzaki, M., & Kazadzis, S. (2024). Effects of clouds and
798 aerosols on downwelling surface solar irradiance nowcasting and short-term
799 forecasting. *Atmospheric Measurement Techniques*, 17(7), 1851–1877.
800 <https://doi.org/10.5194/amt-17-1851-2024>

801 Papachristopoulou, K., Fountoulakis, I., Gkikas, A., Kosmopoulos, P. G., Nastos, P. T., Hatzaki,
802 M., & Kazadzis, S. (2022). 15-year analysis of direct effects of total and dust aerosols in solar
803 radiation/energy over the Mediterranean Basin. *Remote Sensing*, 14(7), 1535.
804 <https://doi.org/10.3390/rs14071535>

805 Paulescu, E., & Blaga, R. (2019). A simple and reliable empirical model with two predictors for
806 estimating 1-minute diffuse fraction. *Solar Energy (Phoenix, Ariz.)*, 180, 75–84.
807 <https://doi.org/10.1016/j.solener.2019.01.029>

808 Pedro, H. T. C., Inman, R. H., & Coimbra, C. F. M. (2017). Mathematical methods for optimized
809 solar forecasting. In *Renewable Energy Forecasting* (pp. 111–152). Elsevier.

810 Pfenninger, S., & Staffell, I. (2016). Long-term patterns of European PV output using 30 years of
811 validated hourly reanalysis and satellite data. *Energy (Oxford, England)*, 114, 1251–1265.
812 <https://doi.org/10.1016/j.energy.2016.08.060>

813 [Raptis, I.-P., Kazadzis, S., Fountoulakis, I., Papachristopoulou, K., Kouklaki, D., Psiloglou, B. E.,](#)
814 [Kazantzidis, A., Benetatos, C., Papadimitriou, N., & Eleftheratos, K. \(2023\). Evaluation of the](#)
815 [solar energy nowcasting system \(SENSE\) during a 12-months intensive measurement campaign](#)
816 [in Athens, Greece. *Energies*, 16\(14\), 5361. https://doi.org/10.3390/en16145361](#)

817

818 Qu, Z., Oumbe, A., Blanc, P., Espinar, B., Gesell, G., Gschwind, B., Klüser, L., Lefèvre, M.,
819 Saboret, L., Schroedter-Homscheidt, M., & Wald, L. (2017). Fast radiative transfer
820 parameterisation for assessing the surface solar irradiance: The Heliosat-4
821 method. *Meteorologische Zeitschrift*, 26(1), 33–57. <https://doi.org/10.1127/metz/2016/0781>

822 Renewables Ninja. (n.d.). *Climate data interface*. GSEE Documentation.
823 <https://gsee.readthedocs.io/en/latest/climatedata-interface/>

824 Ridley, B., Boland, J., & Lauret, P. (2010). Modelling of diffuse solar fraction with multiple
825 predictors. *Renewable Energy*, 35(2), 478–483. <https://doi.org/10.1016/j.renene.2009.07.018>

826 Schroedter-Homscheidt, M., Azam, F., Betcke, J., Hanrieder, N., Lefèvre, M., Saboret, L., &
827 Saint-Drenan, Y. -M. (2022). Surface solar irradiation retrieval from MSG/SEVIRI based on
828 APOLLO Next Generation and HELIOSAT-4 methods. *Meteorologische Zeitschrift*, 31(6), 455–
829 476. <https://doi.org/10.1127/metz/2022/1132>

830 Shettle, E. (1989). Models of aerosols, clouds, and precipitation for atmospheric propagation
831 studies. In *Atmospheric propagation in the UV, visible, IR and mm-region and related system*
832 *aspects* (AGARD Conference Proceedings No. 454). NATO Advisory Group for Aerospace
833 Research and Development.

834 Stoffel, T. (2013). Terms and Definitions. In *Solar Energy Forecasting and Resource*
835 *Assessment* (pp. 1–19). Elsevier.

836 Toledano, C., González, R., Fuertes, D., Cuevas, E., Eck, T. F., Kazadzis, S., Kouremeti, N.,
837 Gröbner, J., Goloub, P., Blarel, L., Román, R., Barreto, Á., Berjón, A., Holben, B. N., & Cachorro,
838 V. E. (2018). Assessment of Sun photometer Langley calibration at the high-elevation sites
839 Mauna Loa and Izaña. *Atmospheric Chemistry and Physics*, 18(19), 14555–14567.
840 <https://doi.org/10.5194/acp-18-14555-2018>

841 WMO. (2021). *Guide to instruments and methods of observation* (WMO-No. 8).
842 https://library.wmo.int/doc_num.php?explnum_id=57838

843 Yang, D. (2019). SolarData package update v1.1: R functions for easy access of Baseline
844 Surface Radiation Network (BSRN). *Solar Energy (Phoenix, Ariz.)*, 188, 970–975.
845 <https://doi.org/10.1016/j.solener.2019.05.068>

846

847

848

849